Published in final edited form as:
J Magn Reson Imaging. 2013 December ; 38(6): 1564–1571. doi:10.1002/jmri.24063.

MR Thermometry in the Human Prostate Gland at 3.0T for Transurethral Ultrasound Therapy

Elizabeth Ramsay, PhD[1,*], **Charles Mougenot, PhD**[2], **Max Köhler, PhD**[3], **Michael Bronskill, PhD**[1,4], **Laurence Klotz, MD**[5], **Masoom A Haider, MD**[6], and **Rajiv Chopra, PhD**[1,4]

[1]Physical Sciences, Sunnybrook Research Institute, Toronto, Ontario, Canada [2]Philips Healthcare, Toronto, Ontario Canada [3]Philips Healthcare, Vantaa, Uusimaa, Finland [4]Department of Medical Biophysics, University of Toronto, Toronto, Ontario, Canada [5]Urology, Sunnybrook Health Sciences, Toronto, Ontario Canada [6]Medical Imaging, Sunnybrook Health Sciences, Toronto, Ontario Canada

Abstract

Purpose—To investigate the spatial, temporal and temperature resolution of a segmented gradient echo echo-planar imaging (EPI) technique as applied to proton resonance frequency (PRF) shift thermometry at 3 T in the human prostate gland, and to determine appropriate sequence parameters for MRI-controlled transurethral ultrasound thermal therapy.

Materials and Methods—Eleven healthy volunteers (age range 23-58) were scanned at 3 T with a 16-channel torso coil to study the behaviour of a gradient echo EPI thermometry sequence. The temperature stability and geometric distortion were assessed for 11 different parameter sets. In a further five volunteers, the prostate T2* was measured.

Results—For all scan parameters investigated, the temperature standard deviation within the prostate was less than 1°C, while the distortion was less than 1 mm. Temperature stability was best with higher TE values (up to 25 ms), larger voxel sizes and lower EPI factors, but this had to be balanced against requirements for good spatial and temporal resolution. Prostate T2* values ranged from 30 ms to 50 ms.

Conclusion—A good balance between temperature stability and temporal/spatial resolution is obtained with TE = 15ms, voxel size = 1.14mm, and EPI factor = 9, resulting in a dynamic scan time of 7.2 s for the nine slices.

Keywords

MR thermometry; thermal therapy; segmented EPI; proton resonance frequency shift; interventional MRI

[*]Corresponding Author: Elizabeth Ramsay, PhD Sunnybrook Research Institute, Physical Sciences 2075 Bayview Avenue, Rm S605 Toronto, Ontario, Canada M4N 3M5 eramsay@sri.utoronto.ca (416) 480-6100 x7482.

INTRODUCTION

The widespread use of prostate specific antigen (PSA) screening and biopsy means that men diagnosed with prostate cancer are of younger age and have more favourable risk disease (1). Although current treatments are effective at treating localized prostate cancer, they are associated with significant long-term complications to sexual, urinary, and bowel function (2). One approach to improve patient quality-of-life is to develop minimally-invasive, image-guided treatments for localized prostate cancer, potentially transforming the management of localized prostate cancer into an outpatient treatment with reduced morbidity. High-intensity ultrasound energy can be delivered precisely to the prostate from minimally-invasive devices inserted into the rectum or urethra (3,4,5,6). MR thermometry can be used to monitor such treatments non-invasively by acquiring quantitative measurements of the temperature distribution in the prostate and surrounding tissues (7,8,9,10,11). This temperature information also has the potential to control the delivery of energy from therapeutic devices and achieve a high degree of spatial treatment precision.

MRI-controlled transurethral ultrasound therapy uses high-intensity ultrasound energy from a multi-element transducer inserted into the prostatic urethra to generate a pattern of thermal coagulation that conforms to a target volume within the gland. Control over the heating is achieved by using multiplanar MR temperature images as input to a feedback algorithm, and requires a temporal resolution of a few seconds (12). In this context, there is a tricky balance between spatial accuracy, rapid acquisition time, full coverage of the prostate, and temperature accuracy (13). Typical gradient echo-based thermometry methods can achieve the required multiplanar coverage and short acquisition times by decreasing TR and, thus, TE but better temperature contrast is achieved when TE is closer to the T2* of the relevant tissues (14). Gradient echo EPI methods for rapid MR thermometry (15,16,17,18) can achieve short acquisition times with TE values in the 10-30ms range and have been shown to be practical for temperature monitoring of externally focused ultrasound treatments in vivo (19,20,21,22).

In this study, the performance of a segmented gradient echo EPI technique as applied to PRF shift thermometry was assessed at 3 T in the prostate glands of healthy human volunteers. The temperature stability was evaluated for different temporal and spatial resolutions and for a range of echo times by calculating the pixel-by-pixel standard deviation in temperature during a dynamic series of thermometry images. The magnitude of distortion found in EPI thermometry images were also investigated. The ultimate goal was to determine which segmented gradient echo EPI parameters meet the minimum requirements for MRI-controlled transurethral ultrasound therapy at 3 T which are: a temporal resolution less than 10 s for the entire prostate, a spatial resolution 1-2 mm, and a temperature standard deviation less than 1-2°C.

MATERIALS AND METHODS

Subjects

A total of 16 healthy male volunteers ranging in age from 23 to 58 underwent MR imaging of the prostate gland after providing written informed consent for this study, which was

approved by the institutional Research Ethics Board. Eleven volunteers participated in an investigation of the effects of TE, EPI factor and spatial resolution on the temperature standard deviation of MR thermometry. In five other volunteers, T2* mapping of the prostate was performed. All MR imaging was performed on a 3T Achieva (Philips Healthcare, Best, Netherlands; maximum gradient strength = 80 mT/m, maximum slew rate = 200 mT/m/ms) using a 16-channel receive array (Philips SENSE XL Torso Coil). Participants fasted overnight and used the washroom before the morning imaging sessions in order to minimize artifacts arising from intestinal or prostate motion, or from susceptibility effects due to gas in the rectum. Despite these precautions, temperature standard deviation values as high as 5-10°C were observed in some volunteers, and the data of five participants had to be discarded or only partially analyzed.

MRI protocol

Nine slightly oblique (15°) transverse images were acquired through the prostate gland of supine subjects (Figure 1a). A previous human study at 1.5 T (23,24) determined that an ~15° rotation of the transverse plane about a right-left axis would orient slices approximately perpendicular to the transurethral device. Full prostate treatment utilizes up to nine collinear 5 mm ultrasound transducer elements, with the thermometry slices aligned perpendicular to each element. A field-of-view (FOV) of 256 × 256 mm^2 was sufficient cover the body size of all volunteers in the AP direction, while the RL frequency encode direction prevented wrap in that direction. Parallel imaging techniques were not investigated in this study.

For the first eleven volunteers, a T2-weighted TSE anatomical scan (TR/TE = 3411 ms/120 ms, ETL = 26, slice thickness = 5 mm) was acquired, followed by a series of standard Philips segmented gradient echo EPI thermometry sequences with 11 different parameter sets (Table 1). Each thermometry scan consisted of a series of 20 dynamic sets of complex images (Figure 1b,c) with scan times ranging from 2.87 s to 8.00 s. Nine of the eleven thermometry scans were acquired with a matrix of 128 × 128 (voxel size 2.00^2 mm^2), while increased spatial resolution was investigated with matrices of 176 × 176 and 224 × 224 (voxel sizes 1.45^2 mm^2 and 1.14^2 mm^2, respectively). Although the prostate gland itself contains little fat, all thermometry scans used a PROSET 1331 pulse to suppress fat, in order to avoid the shifting of fat signal from outside the prostate into the gland by the EPI chemical shift artifact. The use of PROSET limited the minimum slice thickness to 5.3 mm and mandated an overlap of −0.3 mm in order to centre an MR slice on each 5 mm transducer. To examine the effect of TE on the temperature standard deviation, five scans were performed with an EPI factor of 9, TE values varying from 7 ms to 25 ms and a fixed TR of 180 ms (for 9 slices) chosen to accommodate the largest TE value. Four scans were performed to investigate EPI factors of 5, 9, 13, and 17; these scans used a fixed TE of 15 ms, a fixed phase encoding bandwidth of 66.8 Hz/pixel (the maximum possible at the highest EPI factor) and the shortest possible TR value. Echo spacing ranged from 0.8 ms for an EPI factor of 17, to 2.3 ms for an EPI factor 5. For all 11 parameter sets, the flip angle was chosen to be the Ernst angle, assuming a prostate T1 of 1000 ms at 3 T (25). RF spoiling was used for all thermometry scans, and the k-space acquisitons were symmetric. Magnitude and phase images were reconstructed by linear combination of the separate coil

data into a single channel, without using coil sensitivity maps. Parameters are summarized in Table 1.

Data for T2* measurement was collected using a multi-echo gradient echo EPI sequence with TR = 475 ms, flip angle = 75°, EPI factor = 9 and eight TE values (6.91 ms-87.41 ms). The same nine slice geometry described above was used with a 224 × 224 matrix, resulting in an in-plane resolution of 1.14^2 mm^2. Scan duration was 63 s. The calculation of T2* maps was performed using an analysis and fitting software package developed by Philips and written in IDL (Interactive Data Language, Research Systems, Boulder, CO, USA). The algorithm used in this software performed a least squares non-linear T2* fit on the complex data, incorporating a correction for through-plane field gradients.

Temperature Standard Deviation Assessment

Temporal standard deviation maps were calculated for each of the thermometry scans. These maps were indicative of the uncertainty of temperature over time and also gave a sense for the spatial distribution of temperature uncertainty within the prostate gland. When no heating is applied, the temperature standard deviation maps should ideally match the theoretical temperature uncertainty calculated directly from the phase difference (based on Equation 1 below) .

The first step in calculating the temperature standard deviation maps was to calculate a temporal series of temperature maps using the dynamic series of phase images (26):

$$\Delta T(t) = \frac{\varphi(t) - \varphi_o}{\alpha \quad \gamma B_o TE} \quad [1]$$

where α is the PRF coefficient of −.0095 ppm/°C(16,18,26), γ is the proton gyromagnetic ratio, B_o is the magnetic field, and TE is the echo time. The first five dynamic phase image sets were averaged to calculate a baseline phase image ϕ_o, which was then subtracted from subsequent phase images $\phi(t)$ to create 15 dynamic temperature maps $\Delta T(t)$. Temporal phase unwrapping was also performed during this calculation.

Voxels with a signal-to-noise ratio (SNR) below 10 were masked out in all images in order to remove voxels with unreliable phase information from the analysis. Noise for this calculation was estimated from the difference of magnitude images adjacent in time because the torso filled almost the entire FOV. The average temperature in the masked temperature maps was used to correct for temperature drift over time. Temperature standard deviation maps were created by calculating, on a voxel-by-voxel basis, the standard deviation of the temperature over all images in the dynamic time series using in-house MATLAB code (Mathworks Inc., Natick, MA, USA). Thus one standard deviation map encapsulates the behaviour over the entire time series for the slice in question

Regions of interest (ROI's) were drawn on the standard deviation maps in the prostate region, avoiding any localized artifacts from motion or air in the rectum. This approach focused on the effects of sequence parameters while avoiding confounding issues such as physiological motion and susceptibility artifacts. The mean value of the voxels within the

ROI indicated the mean temperature variation in the region, while the standard deviation of voxels within the ROI provided an error estimate and also reflected the spatial variation of temperature. This analysis was performed for all slices containing significant amounts of prostate tissue and an average was calculated over slices, weighted according to the number of voxels selected in each slice.

Spatial Distortion Assessment

The measure of distortion used was based on Zeng et al (27), whereby the distorted image density ρ_1 can be expressed as a function of the undistorted density ρ by

$$\rho_1(x_1, y_1) = \rho\left(x \pm \frac{\gamma \Delta B(x,y)\,\Delta t}{\Delta k_x}, y + \frac{\gamma \Delta B(x,y)\,T}{\Delta k_y}\right) \quad [2]$$

where γ is the proton gyromagnetic ratio, ΔB is the field inhomogeneity, Δt is the time between adjacent points along k_x, T is the time between adjacent k_y lines, Δk_x and Δk_y are the k_x and k_y step sizes respectively. Since in EPI sequences $T >> \Delta t$, the distortion along y will dominate:

$$\Delta y = y_1 - y = \frac{\gamma \Delta B(x,y)\,T}{\Delta k_y} = \frac{\Delta \varphi(x,y)\, y_{res}}{2\pi \quad TE \quad BW_{pe}} \quad [3]$$

where BW_{pe} is the bandwidth in the phase encoding direction, y_{res} is the spatial resolution in the phase encoding direction, and $\Delta\varphi(x,y)$ is the spatially unwrapped phase difference at location (x,y) arising from the spatial field inhomogeneity $\Delta B(x,y)$.

ROI's covering the whole prostate were defined on magnitude images and then applied to spatially unwrapped phase images at each time point of the dynamic series. Eq 3 was used to determine the distortion Δy in mm at each voxel, and the difference between the maximal positive and the minimal negative displacement values was calculated for voxels within each ROI for each member of the dynamic series. The resulting maximal distortion values were averaged over points in the dynamic time series to yield an average distortion metric and associated standard deviation. The calculation was performed using thermal map and distortion analysis tools developed by Philips Finland and written in IDL. To obtain a single value for each subject, a weighted average over all slices containing significant prostate volume was calculated.

RESULTS

Figure 2 shows a series of typical temperature standard deviation maps (top row) for one volunteer compared to the equivalent anatomical T2-weighted TSE images (bottom row). The prostate temperature standard deviation is very low throughout the prostate, despite considerable intensity variation in the anatomical images. Near the bladder and rectum however, artifacts from air and motion can cause much greater temperature standard deviation (white arrows in Fig 2).

Temperature standard deviation results are shown in Figure 3(a, b) where different symbol colors indicate the averaged results for each of the volunteers whose data could be analyzed. For all cases the temperature standard deviation was less than 1°C. Temperature standard deviation decreased with increasing TE (Fig 3a) in this range of echo times (7-25 ms). Since TR was constant in this part of the study, the magnitude image SNR and scan time was approximately constant for TE values. If this constraint were removed and minimum TR was prescribed for each TE, the results might be somewhat different, and as well, any improvements in temperature standard deviation with increasing TE would have to be balanced against the increased scan time. A gradual increase in temperature standard deviation occurred with increasing EPI factor (Fig 3b) but values remained ≤ 0.5°C for all four EPI factors. A weak trend toward increased distortion with increased EPI factor was observed (Fig 3c) but, in all cases, the distortion was in the sub-millimetre range.

Temperature standard deviation maps for in-plane resolutions of 2.00 mm, 1.45 mm and 1.14 mm (Fig 4a-c) indicate that as the voxel size decreased, the prostate boundaries became better defined but the temperature standard deviation increased. The graph in Fig 4d shows the latter effect quantitatively for the 6 volunteers (different colours) whose data were available for analysis. Temperature standard deviation increased with decreasing voxel size but notably remained less than 1°C even for the smallest voxel size evaluated (1.14 mm).

Figure 5 shows a typical T2* map of a prostate, as well as a graph of the average T2* for each of the five volunteers. This average was calculated over the prostate volume, avoiding the rectum. From this data, it is clear that there is considerable T2* inhomogeneity within any given the prostate, as well as amongst the different volunteers. Averaged T2* values ranged from 30 to 50 ms, with standard deviations of 15-25%.

DISCUSSION

The temperature standard deviation decrease observed with increasing TE is consistent with prostate T2* values of 30-50 ms measured in five volunteers (Fig 5). However, the significant variation in T2* observed would suggest that a single optimal TE value for all prostates cannot be found. Although the lowest temperature standard deviation should be obtained with TE ≈ T2* (14), the values are already quite low at TE = 20 ms and changing slowly. Increasing TE to 35-50 ms would probably yield only modest improvements in temperature standard deviation (<10%), while requiring significantly longer (~50%) acquisition times.

For the scans with varying EPI factor, the minimum TR value and fixed phase encoding bandwidth was used in each case, resulting in shorter readout duration and lower magnitude image SNR as the EPI factor increased. The increase in temperature standard deviation observed (Fig 3b) with increasing EPI factor can thus be accounted for. In choosing an EPI factor, a balance must be struck between the shorter scan times obtainable with higher EPI factors and the greater temperature accuracy characteristic of lower EPI factors.

Another important factor to consider when evaluating EPI factors is spatial distortion. Based on Eq 3 and the fact that y_{res}, TE and the phase encoding bandwidth were fixed for all four

EPI factors investigated, it is not surprising that very little change in distortion with EPI factor was observed. In this study, a common phase encoding bandwidth was chosen to accommodate the highest EPI factor used. It would have been possible to use higher phase encoding bandwidth for the lower EPI factors, resulting in even smaller geometric distortions for those values. Conversely, at higher EPI factors, the maximum available phase encoding bandwidth would necessarily decrease as the time needed for the entire readout train increased, resulting in higher spatial distortions for very high EPI factors. For the purposes of this study, the important point is that for all EPI factors studied, the distortion was less than 1 mm (Fig 3d), which is less than the dimension of the smallest pixel used. Low distortion values are not unexpected because the prostate is a relatively small organ well-centered in the magnet and FOV. Variation between subjects is most likely due to local artifacts caused by intestinal motion and rectal gas.

Typical temperature standard deviation maps for three different voxel sizes are shown in Fig 4. With increasing spatial resolution, the boundaries of the prostate are more clearly defined, which is valuable in the monitoring and successful execution of thermal treatment, particularly when using feedback control. The acquisition time increases with spatial resolution, however, and increases in both the magnitude of the standard deviation and its spatial variation are also apparent. There is clearly a trade-off between the good spatial definition of the prostate boundaries seen with small voxels versus the penalties of larger temperature standard deviations and longer acquisition times. These data strongly suggest that the voxel sizes as low as 1 mm^2 can be used without the temperature standard deviation exceeding 1°C.

In several volunteers for this study (30-40%), artifacts arising from rectal gas and faeces were significant enough to make reliable temperature measurement difficult or impossible. The typical artifact was a dipolar field at the prostate-rectum interface, which led to strongly wrapped phase extending into the prostate. In some cases this was present in all images, while in other cases the effect was transient in time or present only on some slices. It was strong enough to correspond to temperature increases of up to 10°C, sometimes extending across the entire prostate. However, excellent thermometry results were achieved in over half of the minimally prepared volunteers of this study, and artifacts should be less likely in cancer patients undergoing transurethral thermal for several reasons. Patients will have spinal anaesthesia, and the presence of the transurethral applicator and an endorectal cooling device (ECD) will also tend to stabilize and immobilize the prostate. Because the water-filled ECD will lie adjacent to the prostate in the rectum, the air interface and associated phase changes will be translated away from the gland itself. Finally, patients will undergo a more thorough pre-treatment preparation than was the case for the volunteers in this study, including an enema and the administration of antispasmodic medication to suppress gastrointestinal activity.

For fixed spatial resolution, the use of parallel imaging would cause the temporal resolution to increase, but the SNR to decrease by a factor of $g*\sqrt{R}$, where R is the acceleration factor and g is the geometry factor. The geometry factor would also introduce some level of inhomogeneous noise to the images. The choice of whether to accept the reduction in SNR in return for greater temporal resolution will depend on the application. For example,

parallel imaging might not be attractive for focal transurethral treatment of small volumes where overall treatment times are short (eg < 30 min) and accuracy is more important than high temporal resolution. However, in other applications where very high temporal resolution in thermometry is an important consideration, parallel imaging would definitely enhance the treatment process and should be investigated.

One limitation of this study was that coil sensitivity data was not used during image reconstruction. The use of this data in future work will improve magnitude SNR and image homogeneity, thus leading to lower and more spatially uniform temperature standard deviations throughout the prostate. Another limitation was that the T1 value of 1000 ms assumed in calculating the Ernst angle is significantly lower than the values found in (25), which were around 1600 ms. The use of flip angles based on a more realistic T1 value could lead to further reductions in the observed temperature standard deviation.

In previous work at 1.5T using spoiled gradient echo sequences for thermometry (23,24), the minimum temperature standard deviations achievable were 1.0°C to 1.5°C with three 10 mm thick slices, and thermometry with practical update times was not possible for 5 mm slices. Some of the improvement obtained here was due to the move from 1.5 T to 3.0 T and some is also due to the use of an EPI-based acquisition strategy where TE values closer to T2* are possible while also keeping temporal update rates acceptable.

In conclusion, for all sets of scan parameters and for all volunteers, the temperature standard deviation within the prostate was less than 1°C, while the distortion was less than 1 mm. Because temperature standard deviation within the prostate was ≤ 1°C under all conditions, the choice of scan parameters involves a balance amongst low temperature standard deviation , acquisition time and spatial resolution. A good choice would be a voxel size of 1.14 mm (for good spatial resolution), TE = 15 ms, and EPI factor = 9. This parameter choice gives a dynamic scan time of 7.2 s for the nine slices, which is suitable for use in MRI-controlled multiplanar transurethral ultrasound treatment of the prostate gland at 3.0 T.

Acknowledgments

The authors wish to thank Jaakko Tölö for support on the quantification of spatial distortion, as well as Harsh Agarwal and Helga van Vroonhoven-Borgen for supplying the T2* scan protocol and analysis tool, respectively.

Grant Support: National Institutes of Health (NIH 1R21CA159550)

REFERENCES

1. Cooperberg MR, Moul JW, Carroll PR. The Changing Face of Prostate Cancer. J Clin Oncol. 2005; 23:8146–8151. [PubMed: 16278465]
2. Potosky AL, Davis WW, Hoffman RM, Stanford JL, Stephenson RA, Penson DF, Harlan LC. Five-year outcomes after prostatectomy or radiotherapy for prostate cancer: the prostate cancer outcomes study. J Natl Cancer Inst. 2004; 96:1358–1367. [PubMed: 15367568]
3. Diederich CJ. Interstitial ultrasound applicators are practical from an engineering perspective for treating large tumours. Int J Hyperthermia. 1996; 12:305–306. [PubMed: 8926398]
4. Gelet A, Chapelon JY, Margonari J, Theillere Y, Gorry F, Cathignol D, Blanc E. Prostatic tissue destruction by high-intensity focused ultrasound: experimentation on canine prostate. J Endourol. 1993; 7:249–253. [PubMed: 8358423]

5. Gelet A, Chapelon JY. High-intensity focused ultrasound experimentation on human benign prostatic hypertrophy. Eur Urol. 1993; 23(Suppl 1):44–47. [PubMed: 7685696]
6. Gelet A, Chapelon JY. Effects of high-intensity focused ultrasound on the human prostate. J Urol (Paris). 1993; 99:350. [PubMed: 8006425]
7. Chen JC, Moriarty JA, Derbyshire JA, Peters RD, Trachtenberg J, Bell SD, Doyle J, Arrelano R, Wright GA, Henkelman RM, Hinks RS, Lok SY, Toi A, Kucharczyk W. Prostate cancer: MR imaging and thermometry during microwave thermal ablation-initial experience. Radiology. 2000; 214:290–297. [PubMed: 10644139]
8. Peters RD, Chan E, Trachtenberg J, Jothy S, Kapusta L, Kucharczyk W, Henkelman RM. Magnetic resonance thermometry for predicting thermal damage: an application of interstitial laser coagulation in an in vivo canine prostate model. Magn Reson Med. 2000; 44:873–883. [PubMed: 11108624]
9. Peters RD, Henkelman RM. Proton-resonance frequency shift MR thermometry is affected by changes in the electrical conductivity of tissue. Magn Reson Med. 2000; 43:62–71. [PubMed: 10642732]
10. Wansapura JP, Daniel BL, Vigen KK, Butts K. In vivo MR thermometry of frozen tissue using R2* and signal intensity. Acad Radiol. 2005; 12:1080–1084. [PubMed: 16112510]
11. Rieke V, Kinsey AM, Ross AB, Nau WH, Diederich CJ, Sommer G, Pauly KB. Referenceless MR thermometry for monitoring thermal ablation in the prostate. IEEE Trans Med Imaging. 2007; 26:813–821. [PubMed: 17679332]
12. Burtnyk M, Chopra R, Bronskill MJ. Quantitative analysis of 3-D conformal MRI-guided transurethral ultrasound therapy of the prostate: theoretical simulations. Int J Hyperthermia. 2009; 25:116–131. [PubMed: 19337912]
13. Chopra R, Wachsmuth J, Burtnyk M, Haider MA, Bronskill MJ. Analysis of factors important for transurethral ultrasound prostate heating using MR temperature feedback. Phys Med Biol. 2006; 51:827–844. [PubMed: 16467581]
14. De Zwart JA, van Gelderen P, Kelly DJ, Moonen CTW. Fast Magnetic-Resonance Temperature Imaging. J Magn Reson B. 1996; 112:86–90. [PubMed: 8661313]
15. Weidensteiner C, Quesson B, Caire-Gana B, Kerioui N, Rullier A, Trillaud H, Moonen CT. Real-time MR temperature mapping of rabbit liver in vivo during thermal ablation. Magn Reson Med. 2003; 50:322–330. [PubMed: 12876709]
16. Stafford RJ, Price RE, Diederich CJ, Kangasniemi M, Olsson LE, Hazle JD. Interleaved echo-planar imaging for fast multiplanar magnetic resonance temperature imaging of ultrasound thermal ablation therapy. J Magn Reson Imaging. 2004; 20:706–714. [PubMed: 15390144]
17. Salomir R, Palussière J, Vimeux FC, de Zwart JA, Quesson B, Gauchet M, Lelong P, Pergrale J, Grenier N, Moonen CT. Local hyperthermia with MR-guided focused ultrasound: spiral trajectory of the focal point optimized for temperature uniformity in the target region. J Magn Reson Imaging. 2000; 12:571–583. [PubMed: 11042639]
18. Salomir R, Vimeux FC, de Zwart JA, Grenier N, Moonen CT. Hyperthermia by MR-guided focused ultrasound: accurate temperature control based on fast MRI and a physical model of local energy deposition and heat conduction. Magn Reson Med. 2000; 43:342–347. [PubMed: 10725875]
19. Quesson B, Laurent C, Maclair G, de Senneville BD, Mougenot C, Ries M, Carteret T, Rullier A, Moonen CT. Real-time volumetric MRI thermometry of focused ultrasound ablation in vivo: a feasibility study in pig liver and kidney. NMR Biomed. 2011; 24:145–153. [PubMed: 21344531]
20. Quesson B, Merle M, Köhler MO, Mougenot C, Roujol S, de Senneville BD, Moonen CT. A method for MRI guidance of intercostal high intensity focused ultrasound ablation in the liver. Med Phys. 2010; 37:2533–2540. [PubMed: 20632565]
21. Köhler MO, Mougenot C, Quesson B, Enholm J, Le Bail B, Laurent C, Moonen CT, Ehnholm GJ. Volumetric HIFU ablation under 3D guidance of rapid MRI thermometry. Med Phys. 2009; 36:3521–3535. [PubMed: 19746786]
22. Mougenot C, Quesson B, de Senneville BD, de Oliveira PL, Sprinkhuizen S, Palussière J, Grenier N, Moonen CT. Three-dimensional spatial and temporal temperature control with MR

thermometry-guided focused ultrasound (MRgHIFU). Magn Reson Med. 2009; 61:603–614. [PubMed: 19097249]

23. Chopra R, Colquhoun A, Burtnyk M, N'djin WA, Kobolevskiy I, Boyes A, Siddiqui K, Foster H, Sugar L, Haider MA, Bronskill M, Klotz L. MR imaging-controlled transurethral ultrasound therapy for conformal treatment of prostate tissue: initial feasibility in umans. Radiology. 2012; 265:303–313. [PubMed: 22929332]
24. Chopra R, Burtnyk M, N'djin WA, Bronskill M. MRI controlled transurethral ultrasound therapy for localized prostate cancer. Int J Hyperthermia. 2010; 26:804–821. [PubMed: 21043572]
25. Liu, W.; Turkbey, B.; Senegas, J.; Remmele, S.; Stehning, C.; Daar, D.; Pang, Y.; Bernardo, M.; Choyke, P. Comparison of Look-Locker and variable flip angle T1 mapping for DCE-MRI in prostate patients at 3T.. Proc 18th Annual Meeting ISMRM; Stockholm. 2010; p. 4766
26. Ishihara Y, Calderon A, Watanabe H, Okamoto K, Suzuki K, Suzuki Y. A precise and fast temperature mapping using water proton chemical shift. Magn Reson Med. 1995; 34:814–823. [PubMed: 8598808]
27. Zeng H, Constable RT. Image distortion correction in EPI: comparison of field mapping with point spread function mapping. Magn Reson Med. 2002; 48:137–146. [PubMed: 12111941]

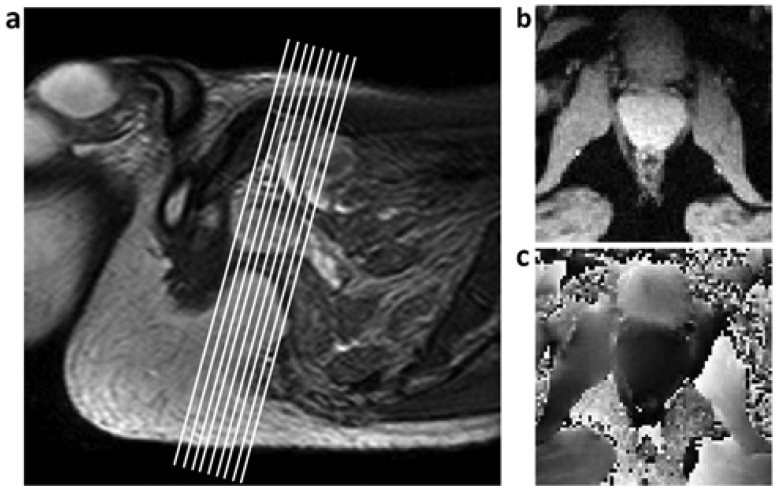

Figure 1.

a) Sagittal image of the pelvic region, showing typical location and orientation of imaging slices. b) Magnitude and c) phase thermometry images cropped to show region around prostate.

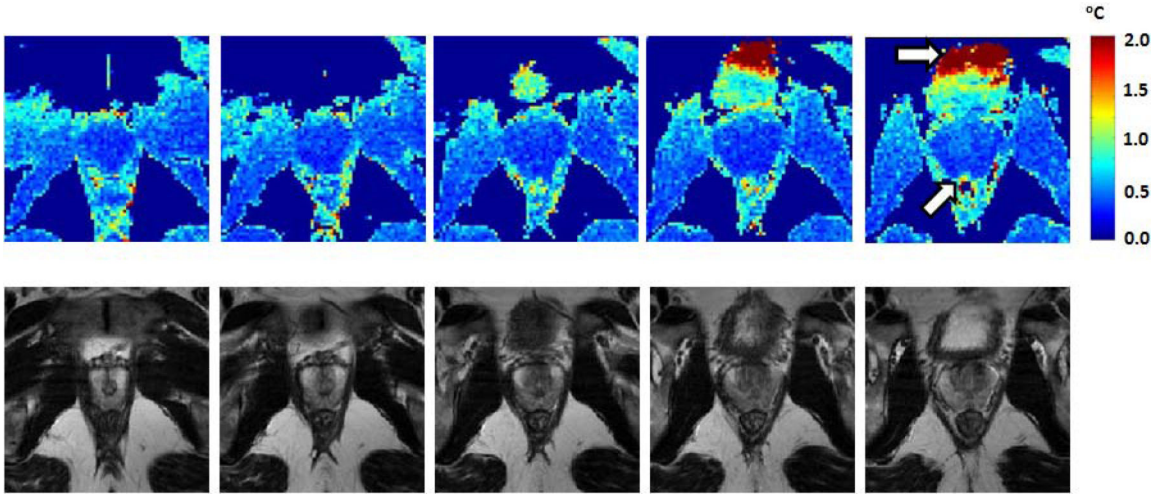

Figure 2.

Typical temperature standard deviation maps for a series of prostate slices (top row) and equivalent T2w anatomical images (bottom row). The white arrows indicate locations in bladder and rectum where the temperature standard deviation is high due to physiologic motion or susceptibility from air.

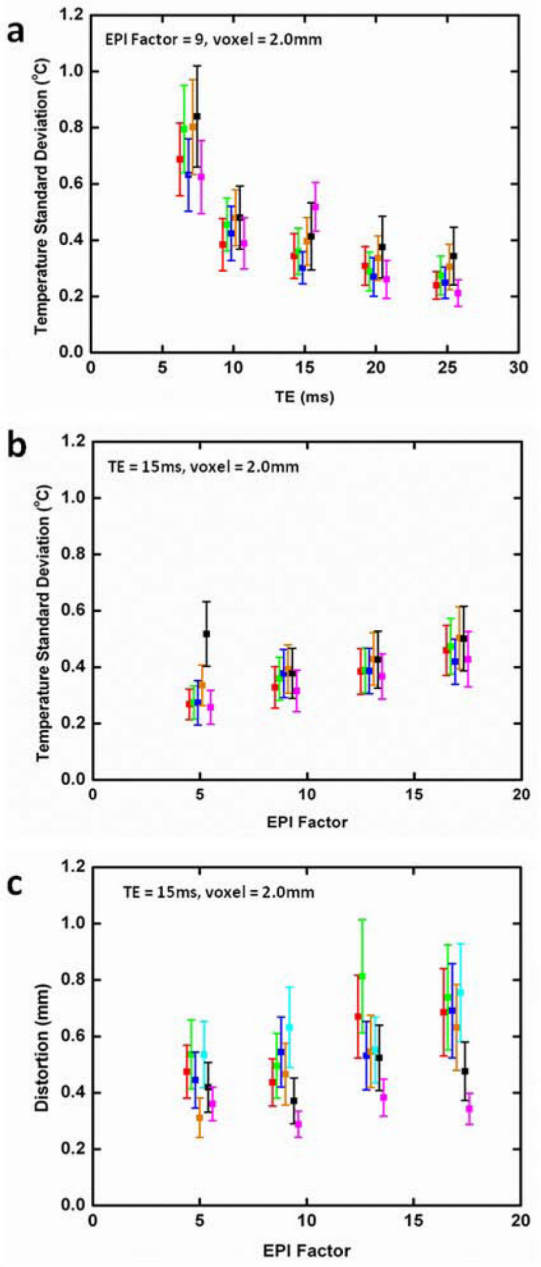

Figure 3.

Average temperature standard deviation as a function of (a) TE and (b) EPI factor. Distortion as a function of EPI factor is shown in (c). In these plots, each symbol color represents results for a different volunteer, averaged in each case over a prostate volume ROI. Values for constant parameters are indicated on each plot.

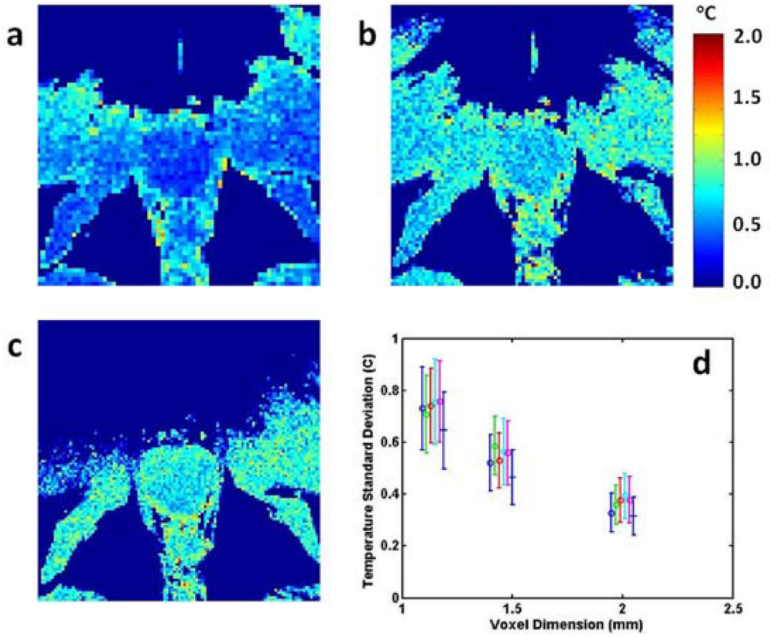

Figure 4.

Temperature standard deviation maps with in-plane spatial resolutions of (a) 2.00 mm, (b) 1.45 mm and (c) 1.14 mm. A plot of temperature standard deviation as a function of voxel dimension is shown in (d). The different colours indicate data from separate volunteers. In all cases, TE = 15 ms and the EPI factor is 9.

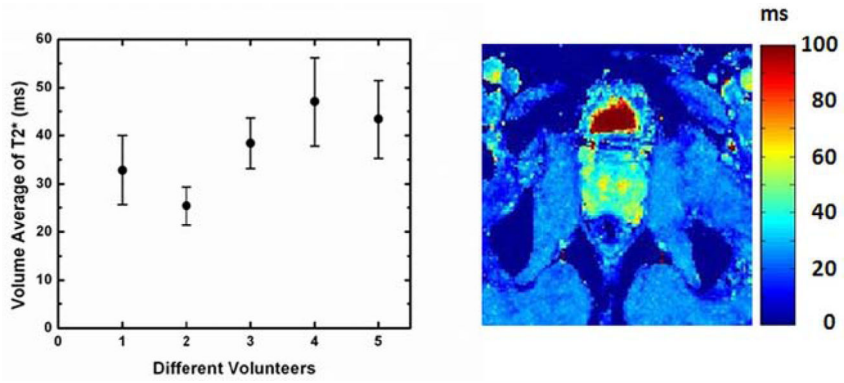

Figure 5.
Average prostate T2* for five different volunteers (left). Typical T2* map (right).

Table 1

Parameters for gradient echo EPI thermometry scans.

Parameter of influence	TR (ms)	TE (ms)	Flip Angle	EPI factor	Bandwidth (Hz/pix)*	Matrix	Voxel size (mm)	Dynamic Time (s)
TE	180	7	33.4	9	114.4	128^2	2.00×2.00	6.55
	180	10	33.4	9	72.4	128^2	2.00×2.00	6.55
	180	15	33.4	9	72.4	128^2	2.00×2.00	6.55
	180	20	33.4	9	72.4	128^2	2.00×2.00	6.55
	180	25	33.4	9	72.4	128^2	2.00×2.00	6.55
EPI Factor	137	15	29.3	5	66.8	128^2	2.00×2.00	8.00
	132	15	28.8	9	66.8	128^2	2.00×2.00	4.77
	130	15	28.6	13	66.8	128^2	2.00×2.00	3.42
	129	15	28.5	17	66.8	128^2	2.00×2.00	2.87
Voxel Size	132	15	28.8	9	66.8	176^2	1.45×1.45	6.14
	132	15	28.8	9	66.8	224^2	1.14×1.14	7.18

Parameters common to all scans: field of view = 256 mm, 9 slices, slice thickness = 5.3 mm, slice gap = −.3 mm.

*Bandwidth in the phase encoding direction